Chemical abundances in Seyfert galaxies – V. The discovery of shocked emission outside the AGN ionization axis

R. A. Riffel [1]★ O. L. Dors [2] M. Armah,[2] T. Storchi-Bergmann,[3] A. Feltre [4] G. F. Hägele,[5,6] M. V. Cardaci [5,6] D. Ruschel-Dutra,[7] A. C. Krabbe,[2] E. Pérez-Montero,[8] N. L. Zakamska [9] and I. C. Freitas[10]

[1]*Departamento de Física, Centro de Ciências Naturais e Exatas, Universidade Federal de Santa Maria, 97105-900 Santa Maria , RS, Brazil*
[2]*Instituto de Pesquisa & Desenvolvimento, Universidade do Vale do Paraíba, Av. Shishima Hifumi, 2911, 12244-000 São José dos Campos Cep, SP, Brazil*
[3]*Instituto de Física, Universidade Federal do Rio Grande do Sul, CP 15051, Porto Alegre , RS 91501-970, Brazil*
[4]*Italian National Institute for Astrophysics – Osservatorio di Astrofisica e Scienza dello Spazio di Bologna, Via P. Gobetti 93/3, I-40129 Bologna, Italy*
[5]*Instituto de Astrofísica de La Plata (CONICET-UNLP),, Argentina*
[6]*Facultad de Ciencias Astronómicas y Geofísicas, Universidad Nacional de La Plata, Paseo del Bosque s/n, 1900 La Plata, Argentina*
[7]*Departamento de Física, Universidade Federal de Santa Catarina, P.O. Box 476, 88040-900 Florianópolis, SC, Brazil*
[8]*Instituto de Astrofísica de Andalucía, Camino Bajo de Huétor s/n, Aptdo. 3004, Granada E-18080, Spain*
[9]*Department of Physics & Astronomy, Johns Hopkins University, Bloomberg Center, 3400 N. Charles St, Baltimore, MD 21218, USA*
[10]*Colégio Politécnico, Universidade Federal de Santa Maria, Santa Maria 97105-900, RS, Brazil*

ABSTRACT

We present maps for the electron temperature in the inner kpc of three luminous Seyfert galaxies: Mrk 79, Mrk 348, and Mrk 607 obtained from Gemini Multi-Object Spectrograph-integral field unit observations at spatial resolutions of ∼110–280 pc. We study the distributions of electron temperature in active galaxies and find temperatures varying in the range from ∼8000 to $\gtrsim$ 30 000 K. Shocks due to gas outflows play an important role in the observed temperature distributions of Mrk 79 and Mrk 348, while standard photoionization models reproduce the derived temperature values for Mrk 607. In Mrk 79 and Mrk 348, we find direct evidence for shock ionization with overall orientation orthogonal to the ionization axis, where shocks can be easily observed as the active galactic nuclei radiation field is shielded by the nuclear dusty torus. This also indicates that even when the ionization cones are narrow, the shocks can be much wider angle.

Key words: galaxies: abundances – galaxies: active – galaxies: ISM – galaxies: Seyfert.

1 INTRODUCTION

Active galactic nuclei (AGNs) present in their spectra strong emission lines whose relative intensities can be used to estimate or characterize the physical and chemical properties of the gas phase in these objects, such as the nature and strength of the interstellar radiation fields, chemical abundance, local temperature, and gas density. The high luminosity of the AGNs continuum and these emission lines have made AGN essential in the studies of chemical evolution of galaxies across the Hubble time. Photoionization models of the narrow line region (NLR) have often been used for determining chemical abundances of heavy elements in AGN host galaxies. The pioneering work by Ferland & Netzer (1983), who used the first version of the photoionization CLOUDY code, showed that NLR exhibits metallicities in the range $0.1 \lesssim (Z/Z_{\odot}) \lesssim 1.0$. Thereafter, several studies exploiting photoionization models have been carried out aiming to estimate the metallicity of AGN host galaxies in the local universe (e.g. Storchi-Bergmann et al. 1998; Feltre, Charlot & Gutkin 2016; Castro et al. 2017) and at high redshifts (e.g. Dors et al. 2018; Mignoli et al. 2019; Guo et al. 2020).

In spite of the wide use of photoionization models in the estimation of gas metallicities, their application in deriving elemental abundances has several limitations. First, it is necessary to assume an incident spectral energy distribution as one of the input parameters of the models, which is generally represented by the power-law component of the non-thermal X-ray radiation with continuum between 2 keV and 2500 Å with a spectral index α_{ox} (Marchese et al. 2012; Dors et al. 2019). Detailed photoionization models used to derive O and N abundances (Dors et al. 2017) and Bayesian-like approach (Pérez-Montero et al. 2019) have predicted α_{ox} to be higher than −1.2 for Seyfert 2 nuclei. Conversely, measurements of α_{ox} by Miller et al. (2011) indicate that most AGNs have α_{ox} of the order of −1.4 and even lower values (∼−2.0) can be derived for these objects. This indicates that an extra physical process is missing in the models (probably shocks; e.g. Contini 2019). Additionally, the use of emission line intensities observed in a limited spectral range can produce a degeneracy in the models (e.g. Davies et al. 2014) and, consequently, uncertainties in the chemical abundance values.

Direct determination of abundances, known as the T_e-method that is based on the observational determination of the electron temperature (T_e), yields more reliable abundance estimations because
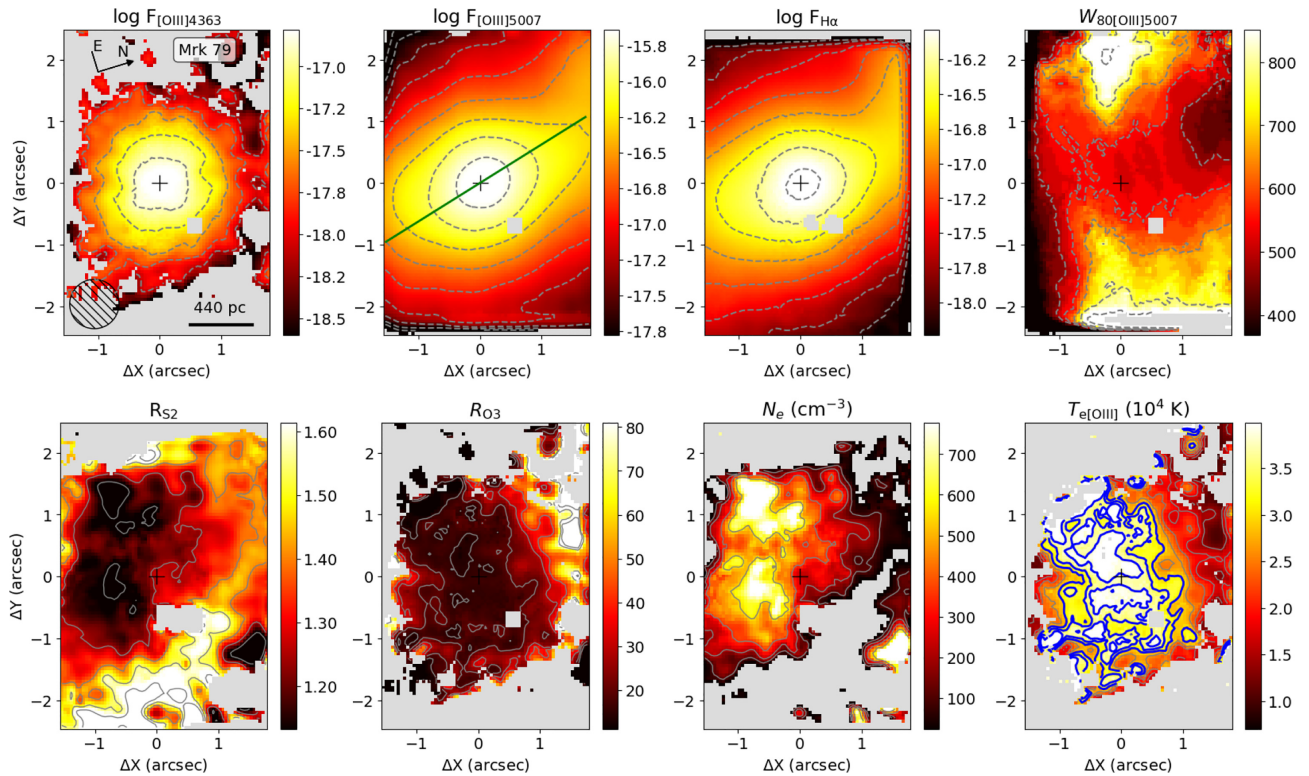
★ E-mail: rogemar@ufsm.br

Figure 1. Maps for Mrk 79, which has a bolometric luminosity of $\log L_{\mathrm{bol}}/(\mathrm{erg\,s^{-1}}) = 45.0$ and a distance of $d = 91.6\,\mathrm{Mpc}$ (see Freitas et al. 2018). Top row: Emission-line flux distributions and W_{80} map for the [O III]5007 emission line. Bottom row: flux line ratios, N_{e} and $T_{\mathrm{e[O\,III]}}$ maps. The central crosses mark the position of the continuum peak, the circle shows the seeing disc, the spatial scale and orientation are shown in the [O III]λ4363 flux map. Grey regions correspond to locations where the emission lines were not detected with a S/N > 3. The contours show the levels of each map. Blue contours in the $T_{\mathrm{e[O\,III]}}$ map correspond to values larger than 30 000 K, where the uncertainties using R_{O3} to derive $T_{\mathrm{e[O\,III]}}$ are large. The green line on the [O III] flux maps shows the orientation of the AGN ionization axis, as obtained from *HST* images by Schmitt et al. (2003).

it circumvents the aforementioned problems of photoionization models. Recently, Dors et al. (2020) presented a new methodology for the T_{e}-method to be applied to NLRs of Seyfert 2 nuclei, introducing a new relation between temperatures of the low (t_2) and high (t_3) ionization gas zones derived from photoionization models. This method produces O/H abundances slightly lower (about 0.2 dex) than those derived from detailed photoionization models. However, previous studies have questioned the use of the T_{e}-method in AGNs. For example, Stasińska (1984) argued that in the NLR the intensity of the [O III](λ4949+λ5007)/λ4363 line ratio, used to derive t_3 (e.g. Hägele et al. 2008), is enhanced by emissions from clouds with high gas density ($N_{\mathrm{e}} \gtrsim 10^5\,\mathrm{cm^{-3}}$), which precludes any direct determination of abundances based on the T_{e}-method. Nagao, Murayama & Taniguchi (2001) found evidence that the [O III]λ4363 line is emitted in denser ($N_{\mathrm{e}} \sim 10^{5-7}\,\mathrm{cm^{-3}}$) and obscured gas regions than those emitting [O III]λ5007.

Shocks from AGN outflows may also affect the ionization structure and T_{e} distribution, particularly in regions where the AGN ionizing photons are shielded by nuclear obscuration (Contini & Viegas 2001; Zakamska & Greene 2014), where the contribution of photoionization to gas ionization is expected to be lower. Spatially resolved measurements of electron temperature and density are important to constrain the AGN contribution to gas ionization and to infer the gas physical conditions. Observational data that enable measurements of weak auroral lines, from which T_{e} can be estimated, and spatially resolved studies of T_{e} in AGNs are seldom found in the literature (but see Revalski et al. 2018; D'Agostino et al. 2019; Dahmer-Hahn et al. 2019).

In this Letter, we present two-dimensional maps of electron temperature and electron density in the NLR, in the case in one Seyfert 1 (Mrk 79) and two Seyfert 2 (Mrk 348 and Mrk 607) galaxies, obtained from integral field spectroscopy. A thorough analysis of T_{e} and N_{e} could be performed with the use of 2D spectroscopy at spatial resolutions of a few hundred parsecs in these three AGN hosts. In Section 2, we describe the data and techniques to derive T_{e} and N_{e}. In Section 3, we present and discuss the results, while the conclusions are given in Section 4.

2 METHODOLOGY

We use the Gemini Multi-Object Spectrograph (GMOS; Allington-Smith et al. 2002) integral field unit data to map the T_{e} and N_{e} in the inner few hundred parsecs of the nearby luminous Seyfert galaxies Mrk 79 (Sy 1, SBb), Mrk 348 (Sy 2, SA(s)0/a), and Mrk 607 (Sy 2, Sa). These galaxies were selected from the sample of Freitas et al. (2018) because they have [O III]λ4363 extended emission. The GMOS data cover the spectral range from 4300 to 7100 Å with a velocity resolution of $\sim$90 km s^{-1} (full width at half-maximum) and spatial resolutions of 280 $\pm$ 30 (Mrk 79), 190 $\pm$ 25 (Mrk 348), and 110 $\pm$ 14 pc (Mrk 607). The data reduction followed the standard procedures using the GEMINI.IRAF package as described by Freitas et al. (2018). We use the IFSCUBE python package (Ruschel-Dutra 2020) to fit the emission-line profiles and obtain the emission-line flux distributions. We allow the fit of up to three Gaussian components per emission line and the line fluxes are obtained by the sum of the fluxes of the individual components (see Supplementary Material).
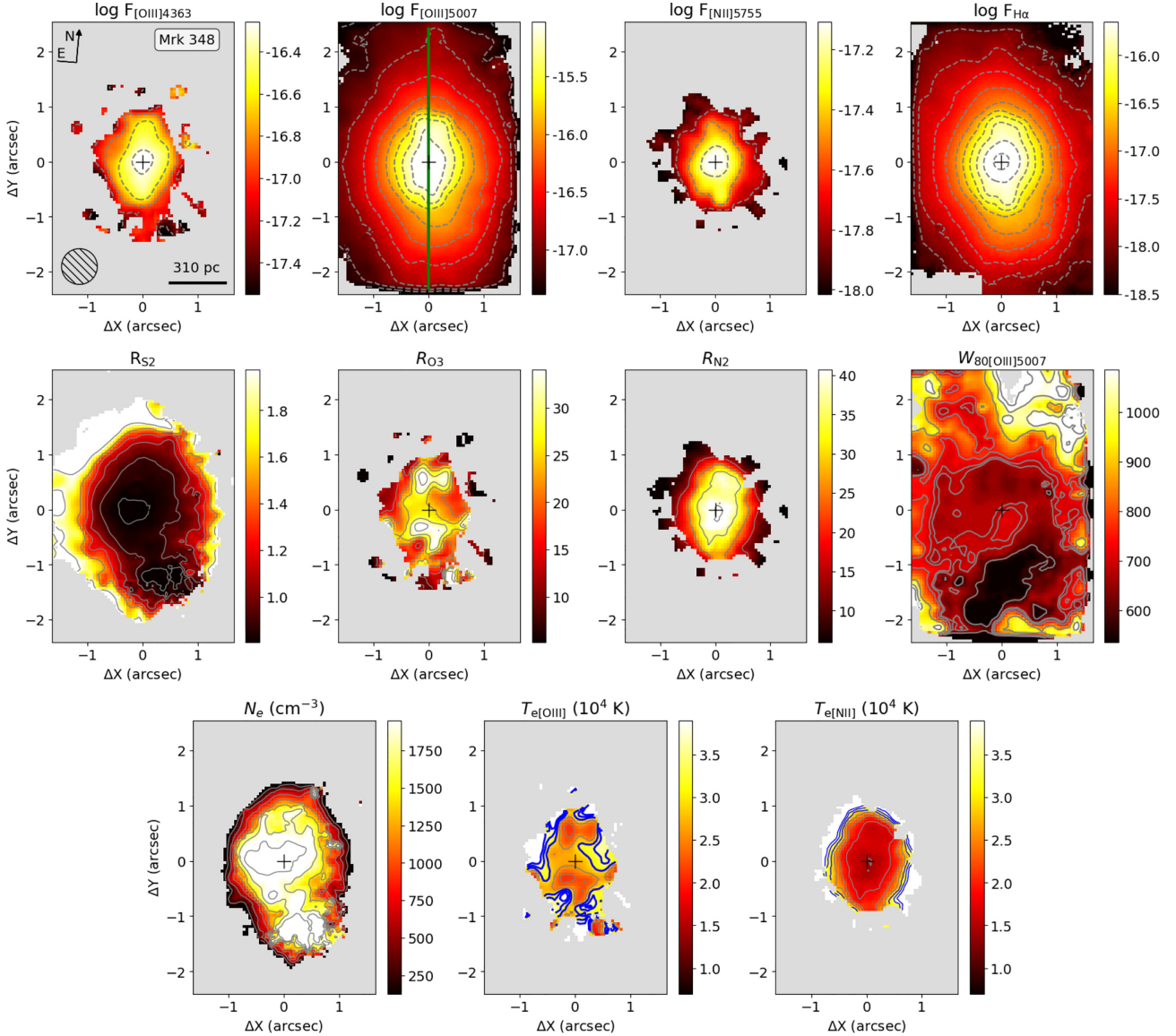
Figure 2. Maps for Mrk 348 [$\log L_{bol}/(\mathrm{erg\,s^{-1}}) = 45.3$, $d = 63.9$ Mpc]. Emission-line flux distributions (top row), flux line ratios and $W_{80[O\,III]}$ (middle row), and N_e, $T_{e[O\,III]}$, and $T_{e[N\,II]}$ maps (bottom row). The labels are the same as for Fig. 1.

We derive the electron temperature using two sets of auroral/nebular line intensity ratios: $R_{O3} = ([O\,III]\lambda\lambda 4959, 5007/\lambda 4363)$ and $R_{N2} = ([N\,II]\lambda\lambda 6548, 6584/\lambda 5755)$, using (Hägele et al. 2008):

$$\frac{T_{e[O\,III]}}{10^4 \mathrm{K}} = 0.8254 - 0.0002415 R_{O3} + \frac{47.77}{R_{O3}} \quad (1)$$

and

$$\frac{T_{e[N\,II]}}{10^4 \mathrm{K}} = 0.537 + 0.000253 \times R_{N2} + \frac{42.13}{R_{N2}}. \quad (2)$$

The [N II]$\lambda 5755$ emission line is not detected for Mrk 79 and, thus, we are unable to calculate the $T_{e[N\,II]}$ for this galaxy.

We estimate the electron density (N_e) from the $R_{S2} = $ [S II]$\lambda 6716/\lambda 6731$ emission-line intensity ratio using the PYNEB routine (Luridiana, Morisset & Shaw 2015), assuming the $T_{e[O\,III]}$ values obtained for each spaxel. For spaxels with no measurements of $T_{e[O\,III]}$, we use the mean $T_{e[O\,III]}$ value for each galaxy.

3 RESULTS AND DISCUSSION

Figs 1–3 show emission-line flux distributions, flux line ratios, electron density, and electron temperature maps for Mrk 79, Mrk 348, and Mrk 607, respectively. The emission-line ratios are corrected for dust extinction, as estimated from the Hα and Hβ fluxes (see Supplementary Material). The flux distributions for [O III]$\lambda 4363$, [O III]$\lambda 5007$, [N II]$\lambda 5755$, and Hα emission lines are shown in the first row of each figure. There is no detection of the [N II]$\lambda 5755$ emission line in the spectra of Mrk 79 and thus, we do not show its flux map for this galaxy. The N_e maps present values in the range ~ 100–2000 cm^{-3}, with the highest values seen at the nucleus for all galaxies. The [Ar IV]$\lambda 4711, 4740$ emission lines trace denser gas phases than the [S II] lines ratio. The [Ar IV] emission is not spatially resolved in our sample, but we measure the [Ar IV]$\lambda 4711/\lambda 4740$ line ratio by integrating the spectra within an 1 arcsec $\times$ 1 arcsec centred at the nucleus. We obtain ratios of 0.64 ± 0.20, 0.44 ± 0.15, and 0.25 ± 0.20, which correspond to densities of $\sim 15\,200$, $31\,700$, and $80\,800$ cm^{-3} for Mrk 79, Mrk 348, and Mrk 607, respectively.
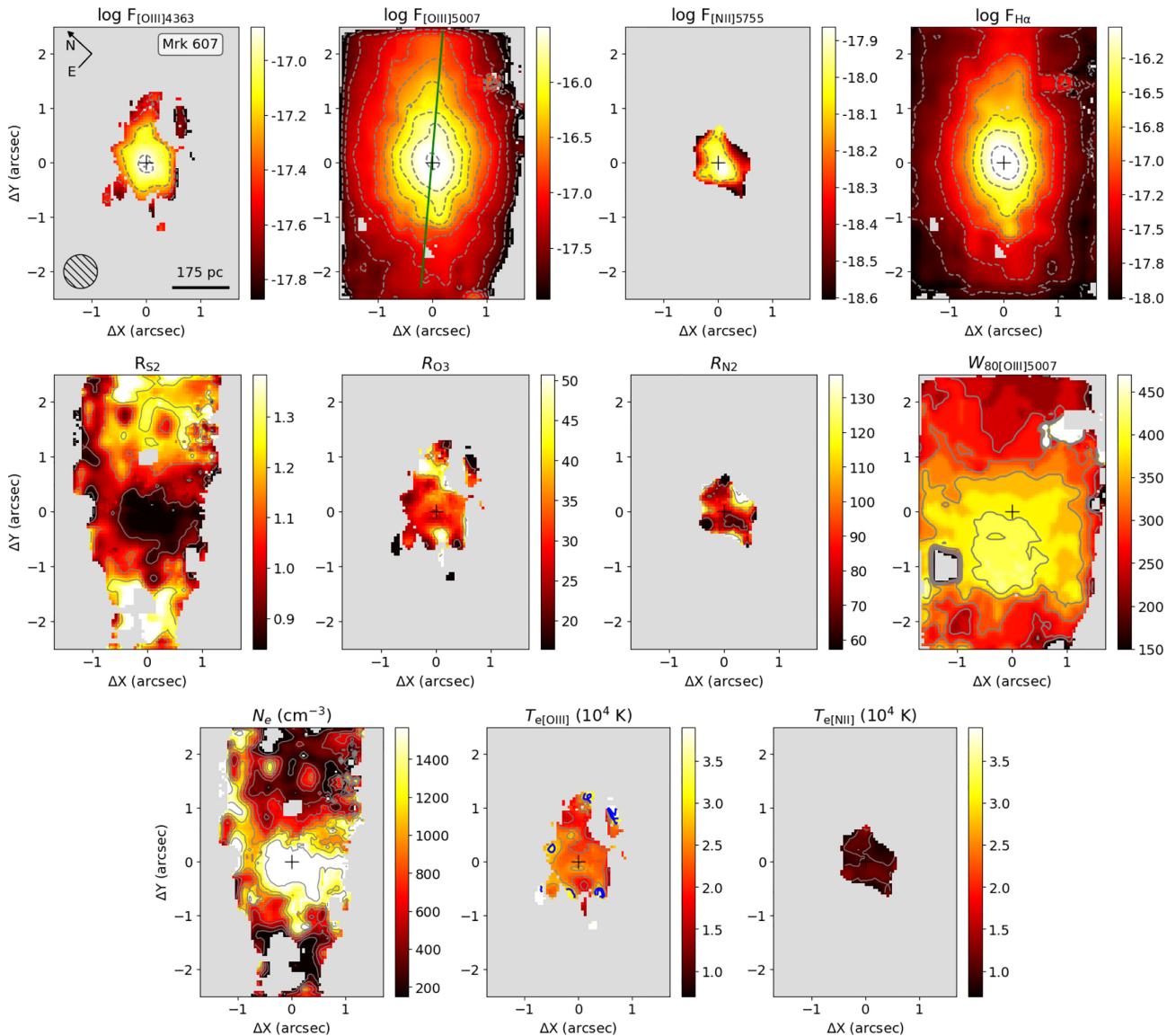
Figure 3. Same as Fig. 2 but for Mrk 607 [log $L_{bol}/(\text{erg s}^{-1}) = 43.4$, $d = 36.1$ Mpc].

The [O III]λ4363 and [N II]λ5755 flux distributions are spatially resolved (see Supplementary Material) in our sample. Thus, we use the fluxes of these lines to compute spatially resolved maps for R_{O3} and R_{N2}. The [S II] emission spreads over most of the GMOS field of view for all galaxies, allowing us to construct R_{S2} maps. We show these maps in Figs 1–3.

The bottom panels of Figs 1–3 show the N_e and T_e maps for Mrk 79, Mrk 348, and Mrk 607, respectively. These properties were computed from the R_{S2}, R_{O3}, R_{N2} following the procedure described in Section 2. In all the galaxies, we find the highest values of R_{O3} along the AGN photoionization structure traced by the [O III]λ5007 emission (Schmitt et al. 2003). Otherwise, smaller R_{O3} values are derived mostly away from the AGN ionization axis, indicating higher temperatures at these locations. This indicates that, besides AGN photoionization, an additional process may be producing the observed emission. There are some differences in the T_e distributions observed in the three objects. For Mrk 348 and Mrk 79, very high temperature values ($\gtrsim 30\,000$ K) are observed in several spaxels. Most of the ionized gas emission in the inner kpc of these galaxies

is produced in outflows with velocities of up to 200 km s^{-1} (Riffel, Storchi-Bergmann & Winge 2013; Freitas et al. 2018). The high-temperature values are likely due to shocks produced by the outflows, hence, the gas reaches a maximum temperature in the immediate postshock region ($T_e \propto V_s^2$, Contini 2019, where V_s is the shock velocity). For Mrk 79, it was possible to estimate T_e in the outskirt regions, where relatively low values (10 000–12 000 K) are derived, which indicate a large temperature gradient in this object. For Mrk 348, the T_e maps show an increase in temperature from the nucleus to locations farther away from it, with $T_{e[\text{N II}]}$ increasing from 8000 to $\gtrsim 30\,000$ K. The $T_{e[\text{O III}]}$ map shows values larger than $\sim 20\,000$ K in most locations, with slightly higher values seen in regions away from the nucleus. The T_e distributions found for Mrk 79 and Mrk 348 are distinct from the findings of Revalski et al. (2018) for Mrk 573 based on long-slit data, where they find no systematic variations in temperature, with a mean value of 13 500 ± 650 K. The $T_{e[\text{O III}]}$ and $T_{e[\text{N II}]}$ maps for Mrk 607 show only small variations in temperature, with $T_{e[\text{O III}]} \sim 20\,000$ K and $T_{e[\text{N II}]} \sim 10\,000$ K. No clear evidence of outflows is seen in this galaxy (Freitas et al. 2018).
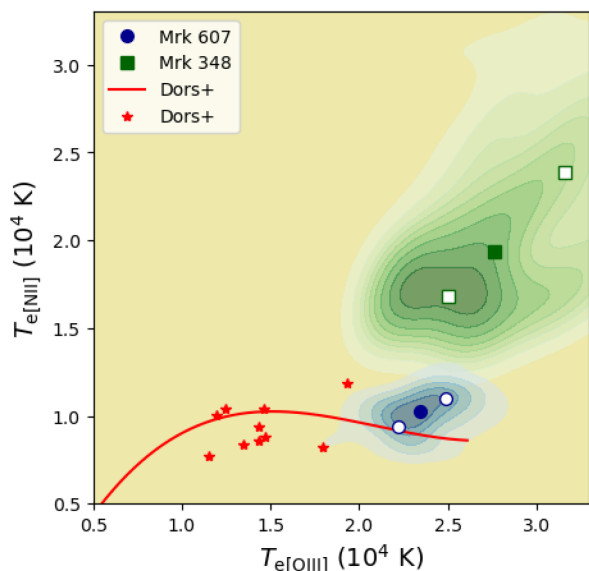
Figure 4. $T_{e[O\,III]}$ versus $T_{e[N\,II]}$. The green and blue density curves are for Mrk 348 and Mrk 607, respectively. The open squares and open circles show the 25th and 75th percentile T_e values for Mrk 348 and Mrk 607, respectively. The filled squares and circles show the median T_e values. The red stars are the AGN compilation of direct estimates of temperatures from Dors et al. (2017, 2020), and the red curve corresponds to predictions of their AGN photoionization models.

Fig. 4 shows the $T_{e[N\,II]}$ versus $T_{e[O\,II]}$ plot with the observed values for Mrk 607 and Mrk 348, which are compared to predictions of AGN photoionization models built with the CLOUDY code (Ferland et al. 2013) by Dors et al. (2020) and to integrated measurements for Seyfert 2 galaxies. While the points for Mrk 607 are seen in the same region occupied by the model predictions and by the integrated spectra, the points for Mrk 348 are located in a very distinct position, towards higher temperatures. This result, together with the fact that the [O III] emission in the nuclear region of this galaxy is mainly due to outflowing gas (Freitas et al. 2018), is a strong indication that outflows have an important effect on temperature structure of AGN hosts. We find that the temperature increases with [O I]6300/Hα, a known tracer of shocks (e.g. Allen et al. 2008; Rich, Kewley & Dopita 2014) and with the width of [O III]5007 (see Supplementary Material), indicating that shocks from AGN winds produce the high temperatures observed in Mrk 79 and Mrk 348.

The spaxels that show the largest values of T_e in our sample are seen approximately perpendicular to the AGN ionization axis (clearly observed in Mrk 79; Fig. 1), indicating that shocks have a larger relative contribution to the line emission at these locations. An increase in the [O III] line width is seen at these locations (Supplementary Material; Freitas et al. 2018), indicating that the outflows are interacting with gas clouds, partially ionizing them, and producing the observed line emission. Photoionized gas is a more efficient emitter of [O III] lines than shock-ionized gas, therefore, a possible shock contribution to the [O III] emission within the AGN ionization structure is overshadowed by the photoionization contribution. This result indicates that the outflows from Seyfert nuclei may have wide-opening angles as observed in luminous AGNs (e.g. Kakkad et al. 2020) and predicted by theoretical models (Wagner, Bicknell & Umemura 2012; Ishibashi, Fabian & Reynolds 2019). Similar outflows in the equatorial plane of the torus have been reported in a few Seyfert galaxies (Riffel, Storchi-Bergmann & Riffel 2014; Lena et al. 2015). The bipolar outflows observed in

some cases (e.g. Crenshaw et al. 2010; Storchi-Bergmann et al. 2010) may be tracing only the photoionized part of the outflowing gas, as shocks are not efficient in the line production, when competing with photoionization (Zakamska & Greene 2014), and thus the outflows are observed within the AGN ionization structure.

4 CONCLUSIONS

We present spatially resolved maps of the electron temperature within the inner few hundred parsecs of the Seyfert galaxies Mrk 79, Mrk 348, and Mrk 607, obtained from integral field spectroscopy. Our results indicate that shocks play an important role in the observed electron temperature distributions, as they can not be reproduced by AGN photoionization models only. This provides a caveat to studies of chemical abundances based on the usual methods for objects with shock/outflows signatures. Not taking this properly into account could yield biased estimates of the gas properties because shocks can produce an electron energy distribution distinct from the Maxwell–Boltzmann distribution. Shocks are more important in regions away from the AGN ionization axis, where they can be easily observed as the AGN radiation field is shielded by the nuclear dusty torus, while within the AGN ionization structure, photoionization is more efficient in producing line emission.

DATA AVAILABILITY

The data used in this paper are available in the Gemini Science Archive under the project code GN-2014B-Q-87.

REFERENCES

Allen M. G., Groves B. A., Dopita M. A., Sutherland R. S., Kewley L. J., 2008, ApJS, 178, 20
Allington-Smith J. et al., 2002, PASP, 114, 892
Castro C. S., Dors O. L., Cardaci M. V., Hägele G. F., 2017, MNRAS, 467, 1507
Contini M., 2019, MNRAS, 488, 4487
Contini M., Viegas S. M., 2001, ApJS, 137, 75
Crenshaw D. M., Kraemer S. B., Schmitt H. R., Jaffé Y. L., Deo R. P., Collins N. R., Fischer T. C., 2010, AJ, 139, 871
D'Agostino J. J. et al., 2019, MNRAS, 487, 4153
Dahmer-Hahn L. G. et al., 2019, MNRAS, 489, 5653
Davies R. L., Kewley L. J., Ho I. T., Dopita M. A., 2014, MNRAS, 444, 3961
Dors O. L. J., Arellano-Córdova K. Z., Cardaci M. V., Hägele G. F., 2017, MNRAS, 468, L113

Dors O. L., Agarwal B., Hägele G. F., Cardaci M. V., Rydberg C.-E., Riffel R. A., Oliveira A. S., Krabbe A. C., 2018, MNRAS, 479, 2294

Dors O. L., Monteiro A. F., Cardaci M. V., Hägele G. F., Krabbe A. C., 2019, MNRAS, 486, 5853

Dors O. L., Maiolino R., Cardaci M. V., Hägele G. F., Krabbe A. C., Pérez-Montero E., Armah M., 2020, MNRAS, 496, 3209

Feltre A., Charlot S., Gutkin J., 2016, MNRAS, 456, 3354

Ferland G. J., Netzer H., 1983, ApJ, 264, 105

Ferland G. J. et al., 2013, Rev. Mex. Astron. Astrofis., 49, 137

Freitas I. C. et al., 2018, MNRAS, 476, 2760

Guo Y. et al., 2020, ApJ, 898, 26

Hägele G. F., Díaz Á. I., Terlevich E., Terlevich R., Pérez-Montero E., Cardaci M. V., 2008, MNRAS, 383, 209

Ishibashi W., Fabian A. C., Reynolds C. S., 2019, MNRAS, 486, 2210

Kakkad D. et al., 2020, A&A, 642, A147

Lena D. et al., 2015, ApJ, 806, 84

Luridiana V., Morisset C., Shaw R. A., 2015, A&A, 573, A42

Marchese E., Della Ceca R., Caccianiga A., Severgnini P., Corral A., Fanali R., 2012, A&A, 539, A48

Mignoli M. et al., 2019, A&A, 626, A9

Miller B. P., Brandt W. N., Schneider D. P., Gibson R. R., Steffen A. T., Wu J., 2011, ApJ, 726, 20

Nagao T., Murayama T., Taniguchi Y., 2001, ApJ, 549, 155

Pérez-Montero E., Dors O. L., Vílchez J. M., García-Benito R., Cardaci M. V., Hägele G. F., 2019, MNRAS, 489, 2652

Revalski M., Crenshaw D. M., Kraemer S. B., Fischer T. C., Schmitt H. R., Machuca C., 2018, ApJ, 856, 46

Rich J. A., Kewley L. J., Dopita M. A., 2014, ApJ, 781, L12

Riffel R. A., Storchi-Bergmann T., Winge C., 2013, MNRAS, 430, 2249

Riffel R. A., Storchi-Bergmann T., Riffel R., 2014, ApJ, 780, L24

Ruschel-Dutra D., 2020, danielrd6/ifscube v1.0

Schmitt H. R., Donley J. L., Antonucci R. R. J., Hutchings J. B., Kinney A. L., 2003, ApJS, 148, 327

Stasińska G., 1984, A&A, 135, 341

Storchi-Bergmann T., Schmitt H. R., Calzetti D., Kinney A. L., 1998, AJ, 115, 909

Storchi-Bergmann T., Lopes R. D. S., McGregor P. J., Riffel R. A., Beck T., Martini P., 2010, MNRAS, 402, 819

Wagner A. Y., Bicknell G. V., Umemura M., 2012, ApJ, 757, 136

Zakamska N. L., Greene J. E., 2014, MNRAS, 442, 784

SUPPORTING INFORMATION

Supplementary data are available at *MNRASL* online.

Figure S1 Examples of [O III]+Hβ (left) and [N II]+Hα (right) emission-line profiles for Mrk 79 (top), Mrk 348 (middle), and Mrk 607 (bottom).

Figure S2 Examples of the Gaussian fits of the Hγ+[O III]λ4363 (top) and [N II]λ5755 (bottom).

Figure S3 Curves of growth for Mrk 79 (left), Mrk 348 (centre), and Mrk 607 (right).

Figure S4 Maps for Mrk 79.

Figure S5 Same as Fig. 4, but for Mrk 348.

Figure S6 Same as Fig. 4, but for Mrk 607.

Figure S7 BPT [O I]-based diagrams for the spaxels with electron temperature measurements for Mrk 79 (left), Mrk 348 (middle), and Mrk 607 (right).

Please note: Oxford University Press is not responsible for the content or functionality of any supporting materials supplied by the authors. Any queries (other than missing material) should be directed to the corresponding author for the article.

This paper has been typeset from a TEX/LATEX file prepared by the author.